Topics in Catalysis (2018) 61:601–609
https://doi.org/10.1007/s11244-018-0959-5

ORIGINAL PAPER

Iron Oxide Nanostructures for the Reduction of Bicarbonate to Solar Fuels

Hanqing Pan[1] · **Kristian R. Martindale**[1] · **Michael D. Heagy**[1]

Published online: 24 April 2018

Abstract

In this study, iron(III) oxide with different sizes and morphologies were synthesized, characterized, and compared for their photocatalytic efficiency in the reduction of bicarbonate to formic acid. The four different Fe_2O_3 species selected for comparison were micron- and nano-particulate Fe_2O_3, goethite (α-FeOOH), and Fe_2O_3 wires. Within the set of four morphologies, we found that Fe_2O_3 wires possessed a significantly greater surface area. Consequently, this high-surface area wire morphology yielded the highest apparent quantum efficiency (AQE) of 5.59 ± 0.2%. When the photocatalytic efficiency of Fe_2O_3 was compared to commercial P25 TiO_2, it was found that the AQE of Fe_2O_3 wires was three times greater than P25 TiO_2. This work presents the first study of Fe_2O_3 structures in the photo-reduction of bicarbonate to formate, yielding ultra-high photon conversion efficiency to a value-added product.

Graphical Abstract

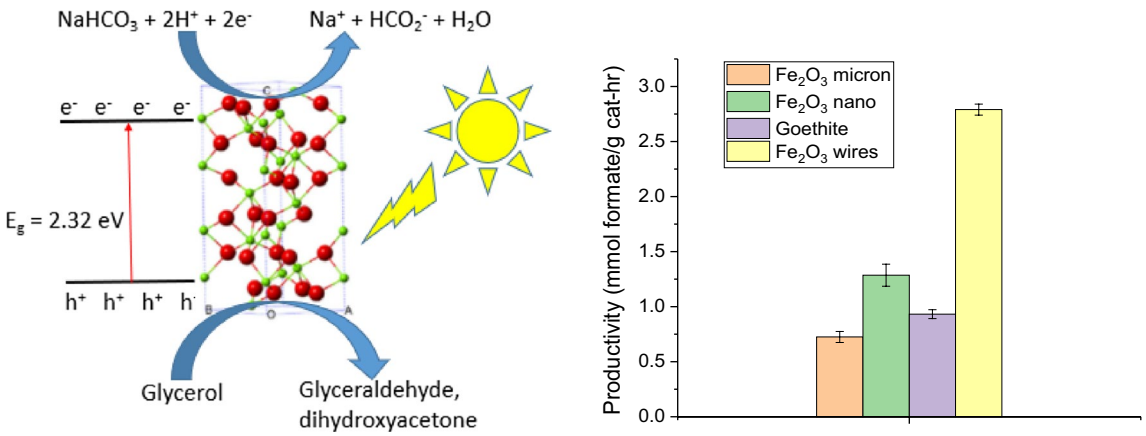

Keywords Chemical carbon mitigation · Iron oxide · Nanowires · Bicarbonate reduction · Solar fuel

The authors dedicate this article in memoriam to Dr. George Andrew Olah for his many inspirational contributions to chemistry and his scientific leadership bequeathed on a global scale to future generations. The advent of his more recently published books such as, *Beyond Oil and Gas: The Methanol Economy*, is largely responsible for the inspiration and findings reported in this article.

Electronic supplementary material The online version of this article (https://doi.org/10.1007/s11244-018-0959-5) contains supplementary material, which is available to authorized users.

✉ Michael D. Heagy
michael.heagy@nmt.edu

1 Introduction

An important area of research for achieving carbon dioxide stabilization targets of 450 ppm or lower, which has gained prominence in light of the Paris Agreement, is the development of negative emission technologies (NETs) [1]. Natural carbon dioxide removal (CDR) sinks such as oceans

[1] Department of Chemistry, New Mexico Institute of Mining and Technology, Socorro, NM 87801, USA

feature prominently toward atmospheric stabilization and have been estimated to uptake annually and store petagram quantities of CO_2 (Pg C). However, studies have shown that on decadal time scales, the ocean may become a less efficient sink for constantly increasing anthropogenic CO_2 [2]. To address such concerns by employing NETs toward the higher concentration of aqueous CO_2 in the form of bicarbonate relative to atmospheric carbon dioxide, the CDR strategy shifts from sequestration to CO_2 utilization. Toward this goal, only solar energy possesses a driving force with comparable magnitude on the order of diurnal terawatts (Tw) to reduce CO_2 and ultimately harness this greenhouse gas for renewable energy, i.e. solar fuels and chemical feedstocks [3].

One potential strategy towards generating renewable fuels employs solar energy to directly reduce atmospheric or locally produced CO_2 to liquid fuels. This approach, referred to as "chemical carbon mitigation" can lead to methanol as an end product, a high-octane fuel. The concept of the "methanol economy", championed by Chemistry Nobel laureate George Olah, highlights methanol as an alternative to hydrogen as a renewable and readily transportable fuel [4]. An important component to the methanol economy comprises the solar-driven conversion of carbon dioxide to formic acid and ultimately to methanol [5, 6]. Methanol, a C1 solar fuel, has higher energy density than compressed hydrogen (Fig. 1), and can therefore store more energy.

Since the discovery of light-induced water splitting with a TiO_2 photoanode in 1972 by Fujishima and Honda [7], and the first report of CO_2 reduction to organic compounds by Inoue et al. in 1979 [8], metal oxides have attracted considerable attention as photocatalyst for water splitting and CO_2 reduction. TiO_2 remains the benchmark semiconductor photocatalyst owing to its abundance, low cost, high reactivity, non-toxicity and stability. Though TiO_2 has been studied extensively, it is a wide band gap photocatalyst (3.2 eV) that absorbs primarily in the UV region, this region accounts for only 4% of the solar spectrum. However, a similar semiconductor such as iron oxide is one of the naturally occurring semiconductors commonly found in soils and sediments [9], is abundant, and non-toxic. Iron oxides have different crystalline structures, including wüstite (FeO), hematite (α-Fe_2O_3), maghemite (ν-Fe_2O_3), magnetite (Fe_3O_4), and goethite (α-FeOOH) [10]. Hematite (α-Fe_2O_3), an n-type semiconductor, is the most stable form of iron oxide under ambient conditions [11], and has many applications in water spitting [12], catalysis [13], gas sensing [14], and solar cells [15].

Iron oxides are transition metal oxides with band gaps (2.1 eV for α-FeOOH [16] and 2.2 eV for α-Fe_2O_3 [17]) that can absorb light up to 600 nm [9]. Such features make them promising candidates for visible-light photocatalysts. α-Fe_2O_3 is naturally abundant, highly stable, inexpensive, resistant to photocorrosion, and environmentally friendly [18–21]. However, Fe_2O_3 has short hole diffusion lengths of 2–4 nm [22, 23], causing photogenerated electrons and holes to recombine too rapidly. By fabricating nanostructures such as rods, plates, wires, and cubes, recombination can be delayed, therefore enhancing photocatalytic activity

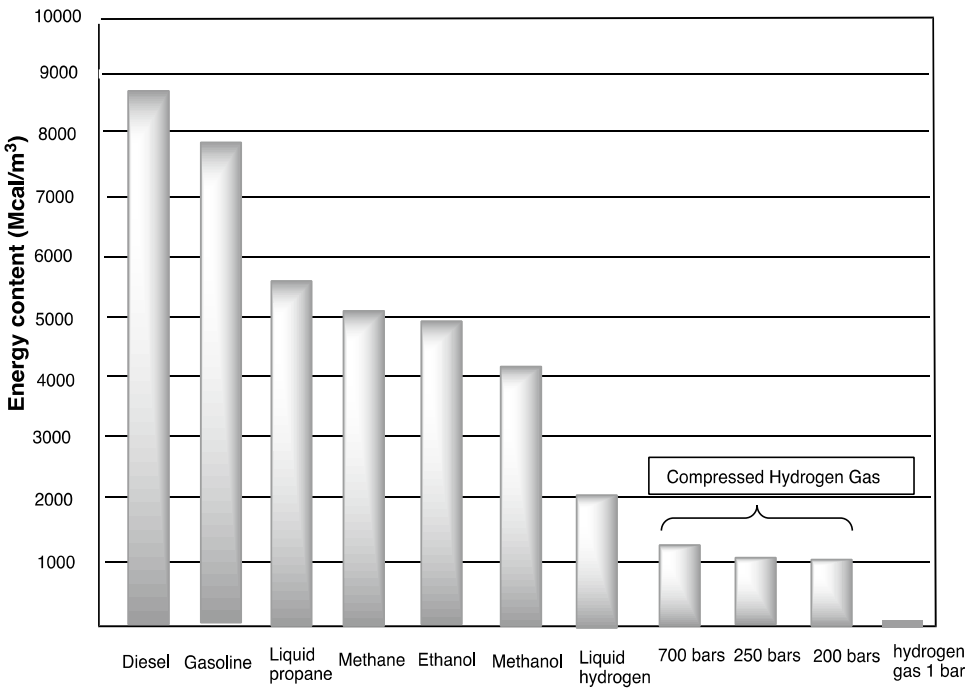

Fig. 1 Energy density of various fuels as compared to compressed hydrogen [4]

[24]. The structures and sizes of this semiconductor can impact its catalytic performance. For example, one-dimensional (1D) nanofibers have high aspect ratios and large surface areas that provide many active sites. These nanofibers are derived by the accumulation of many nanoparticles, which allow photo-induced charge carriers to move easily through grain boundaries, leading to prolonged separation of the electron/hole pair and increased photocatalytic efficiency [11].

Previous applications of Fe_2O_3 include a number of examples in catalysis such as photoelectrochemical materials [12, 25–27], photocatalyst for dye degradation [28–32], CO_2 reduction to CO [33], and water splitting [19]. In this study, we synthesized different sizes and morphologies of Fe_2O_3 for the photocatalytic bicarbonate reduction to formate. We demonstrate the high quantum efficiency of these species by comparing it to commercial P25 TiO_2, and showing that the AQE of Fe_2O_3 wires is three times more than TiO_2. In addition, glycerol is highlighted as a green solvent that readily functions in the capacity of a hole scavenger to react with photogenerated holes, boosting semiconductor efficiency. By combining variations in Fe_2O_3 morphology along with the effect of a reactive hole scavenger, iron oxide is engineered for high photocatalytic performance in the reduction of bicarbonate to formate.

2 Experimental

2.1 Materials

Micron- and nano-particulate Fe_2O_3, goethite, $FeCl_3$, $FeCl_3{\cdot}6H_2O$, nitrilotriacetic acid (NTA) were purchased from Sigma-Aldrich. Isopropanol, NaOH, and urea were purchased from Fisher.

2.1.1 Synthesis of Fe_2O_3 Nanowires [27]

The Fe_2O_3 nanowires were synthesized via a hydrothermal method. Precursors were prepared in the first step in an autoclave. In a typical synthesis, 1.05 mmol $FeCl_3$ was dissolved in 7 mL distilled water and 7 mL isopropanol to form a solution. 3 mmol NTA was then added. After thorough stirring, the mixture was transferred into a Teflon lined autoclave and hydrothermally treated at 180 °C for 24 h. The resultant white floccules were washed with deionized water and absolute ethanol, and dried at 60 °C in a vacuum oven. Finally, the precursors were sintered at 500 °C for 2 h to obtain Fe_2O_3 nanowires.

2.2 Semiconductor Characterization

2.2.1 Size, Crystal Structure, and Surface Area Determination

Crystal structure information was obtained using an X'Pert Pro X-ray diffraction (XRD) instrument. BET surface area measurements were performed on a Micromeritics ASAP 2020 Surface Area and Porosity Analyzer, and scanning electron microscopy (SEM) was performed using a Hitachi S-4100 scanning electron microscope.

2.2.2 Diffuse Reflectance Spectroscopy (DRS)

The dry Fe_2O_3 powders were analyzed by a Thermo Scientific Evolution 260 Bio UV–Vis spectrophotometer with an integrated sphere in order to obtain its band gap. To prepare the sample, 5% of Cu_2O and 95% KBr pellets were mixed and ground using a mortar and pestle. Wavelengths were scanned from 800 to 200 nm. The resulting absorbance spectra were treated to a Kubelka–Munk function plotted against the energy of the incident light to obtain band gap information.

2.2.3 Cyclic Voltammetry

In order to place the band gaps obtained via DRS on an absolute energy scale, cyclic voltammetry was performed using a EDAQ ET014 Echem Electrode kit with an Ag/AgCl reference electrode, platinum wire counter electrode, and a glassy carbon working electrode. The voltage was swept from − 1000 to 1000 mV at a rate of 100 mV/s. The electrolyte used was 0.1 M tetraethylammonium tetrafluoroborate ($TBABF_4$) solution in dry acetonitrile. The procedure for CV was adapted from Fang et al. [34]. For powder samples, suspensions were made of 1 mg/mL in ethanol and sonicated for 1 h to ensure suspension. After sonication, 60 µL of 5% Nafion solution was added to the suspension, and 4.5 µL of the resulting solution was pipette onto a glassy carbon electrode (GCE) and allowed to dry. Several applications of the solution were required to ensure full coverage of the GCE surface [35].

2.2.4 Ion Chromatography

Ion chromatography was performed on a Dionex AS50 IC with a Dionex IonPac ICE-AS6 ion exclusion column and a Thermo Scientific Dionex AMMS-ICE 300 suppressor. The IC instrument is equipped with a Dionex CD25 conductivity detector. Reagents used were 0.4 mM heptafluorobutyric acid as the eluent at a flow rate of 1.2 mL/min and 5 mM tetrabutylammonium hydroxide as the regenerant.

Table 1 Comparison of valence band (VB), conduction band (CB), and band gap of TiO_2 and Fe_2O_3

	TiO_2	Fe_2O_3	
	Literature	Literature [36]	Experimental[a]
VB	3.38	2.9	2.0
CB	0.15	0.58	0.31
Band gap	3.23	2.32	2.31

[a]Experimental values were determined by cyclic voltammetry

2.2.5 Photo-experiments

Reaction matrix: a buffer made of 0.3 M $NaHCO_3$, 2 M hole scavenger (2-propanol or glycerol), and Milli-Q water. Fe_2O_3 catalysts were added at a concentration of 0.1 mg/mL. The matrix was transferred in a quartz tube, sealed, and placed under an ABET Technologies SunLite™ solar simulator with AM 1.5 filter for 8 h. The light source was a 1000 W xenon arc lamp with an output of 1000 W/m^2, the equivalent of 1 sun [3]. Aliquots were collected at 2-h increments, and formate concentration was quantified by ion chromatography.

2.2.6 Apparent Quantum Efficiency (AQE)

Using an Ophir Photonics Nova II laser energy meter, the energy output of the solar simulator was measured. This power measurement was converted to moles of photons per second. This photon flux was then used to calculate the AQE of the catalyst using Eqs. (1) and (2).

$$\text{n mol photons} \times \frac{1 \text{ mol e}^-}{\text{mol photons}} \times \frac{\text{mol formate}}{2 \text{ mol e}^-} = \text{theoretical} \quad (1)$$

$$\frac{\text{Actual mol formate}}{\text{Theoretical mol formate}} \times 100 = \%\text{AQE} \quad (2)$$

3 Results and Discussion

Fe_2O_3 has the advantage of a smaller band gap which allows for visible light absorption (Table 1). The crystal structures of the Fe_2O_3 samples were analyzed by XRD (Supplementary Information S1). Peaks for α-FeOOH are indexed to orthorhombic phase of goethite (with lattice constants a = 0.4596, b = 0.9957, and c = 0.3021 nm). For

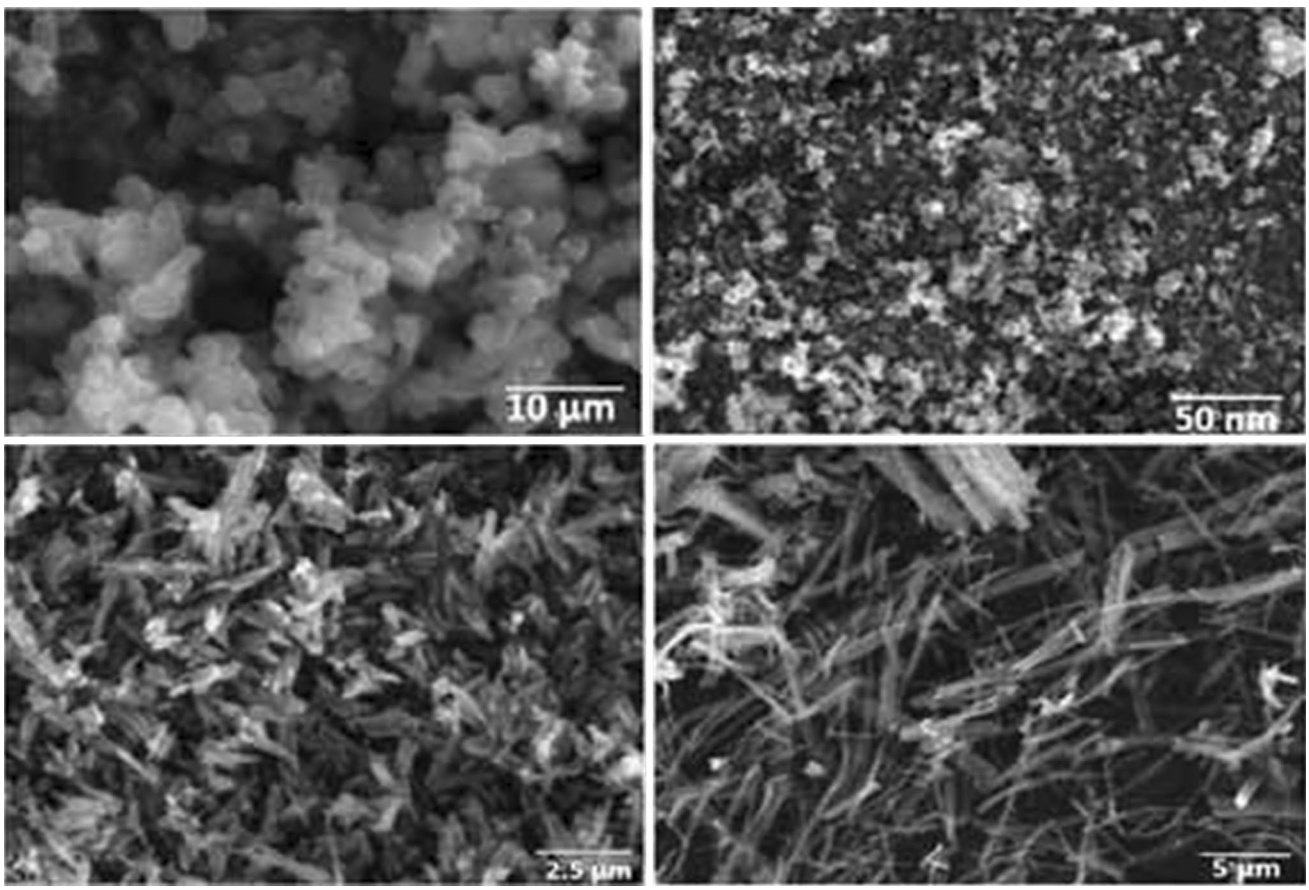

Fig. 2 SEM image of micron- and nano-particulate Fe_2O_3 (top), goethite and Fe_2O_3 wires (bottom)

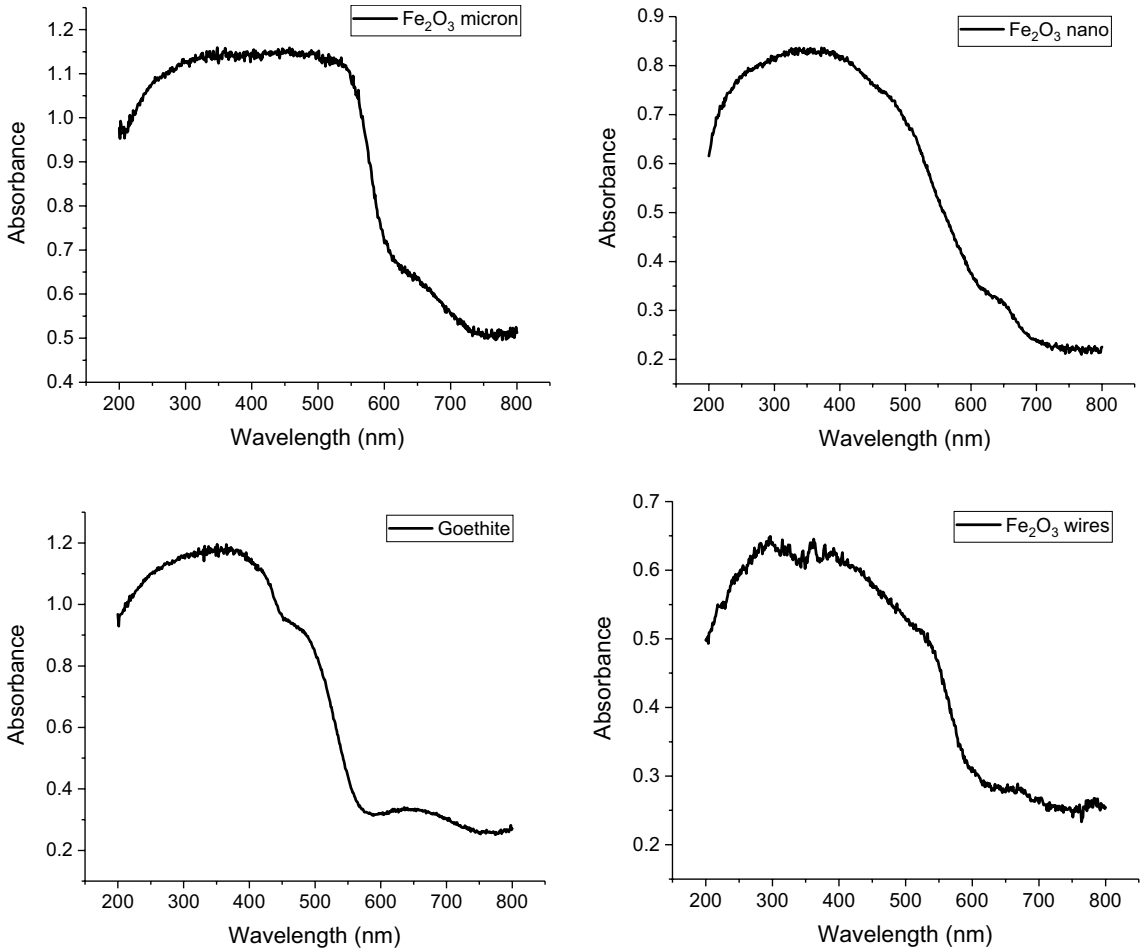

Fig. 3 Diffuse reflectance spectroscopy of micron- and nano-particulate Fe_2O_3 (top), goethite and Fe_2O_3 wires (bottom)

Fe_2O_3 micron and wires the XRD peaks are indexed to a rhombohedral phase (with lattice constants a = 0.5035 and c = 1.3740 nm). Nano-particulate Fe_2O_3 has a tetragonal crystal structure. BET surface area measurements (Table 3) confirm that nano-particulate Fe_2O_3 possesses a greater surface area than micron-sized Fe_2O_3 at 37.367 m^2/g (vs. 20.384 m^2/g for micron Fe_2O_3). Goethite has a surface area of 29.860 m^2/g, and Fe_2O_3 wires exhibit a significantly greater surface area value of 90.130 m^2/g.

The size and morphology of the Fe_2O_3 species can be seen with SEM (Fig. 2). Both micron- and nano-particulate Fe_2O_3 are aggregated, but with sizes of 2 µm and 10 nm (Table 3). Goethite crystals have an elongated rod-like structure with lengths of 2 µm, and Fe_2O_3 wires were 5 µm in length. Although the reduction potential of CO_2/HCOOH is above the conduction band TiO_2 and Fe_2O_3 (Supplementary Information S2), previous work has demonstrated that TiO_2 can reduce CO_2 easily (references). Cyclic voltammetry was used to place band gap values on an absolute NHE scale. Since an Ag/AgCl reference electrode was used, Eq. (3) makes the conversion to normal hydrogen electrode (NHE) values [37]. CV (Supplementary Information S3) confirms that the band gap of Fe_2O_3 is 2.31 eV (Table 1), which is in accordance to the reported value of 2.32 eV.

$$E(NHE) = E(Ag/AgCl) + 0.197\ V \quad (3)$$

Absorbance spectra is obtained using DRS (Fig. 3). Micron- and nano-Fe_2O_3 structures exhibit an absorption band edge near 575 and 500 nm, respectively. For goethite and Fe_2O_3 wires, the absorption band edge occurred near 450 and 550 nm, respectively. The absorbance plot of DRS and subsequent conversion to Kubelka–Munk plot (Fig. 4) can also be used to obtain band gap energies. From DRS, it was determined that the band gap of all Fe_2O_3 structures are approximately 2.1 eV.

With the particles fully characterized, photo-experiments were conducted to test for formate production. Based on

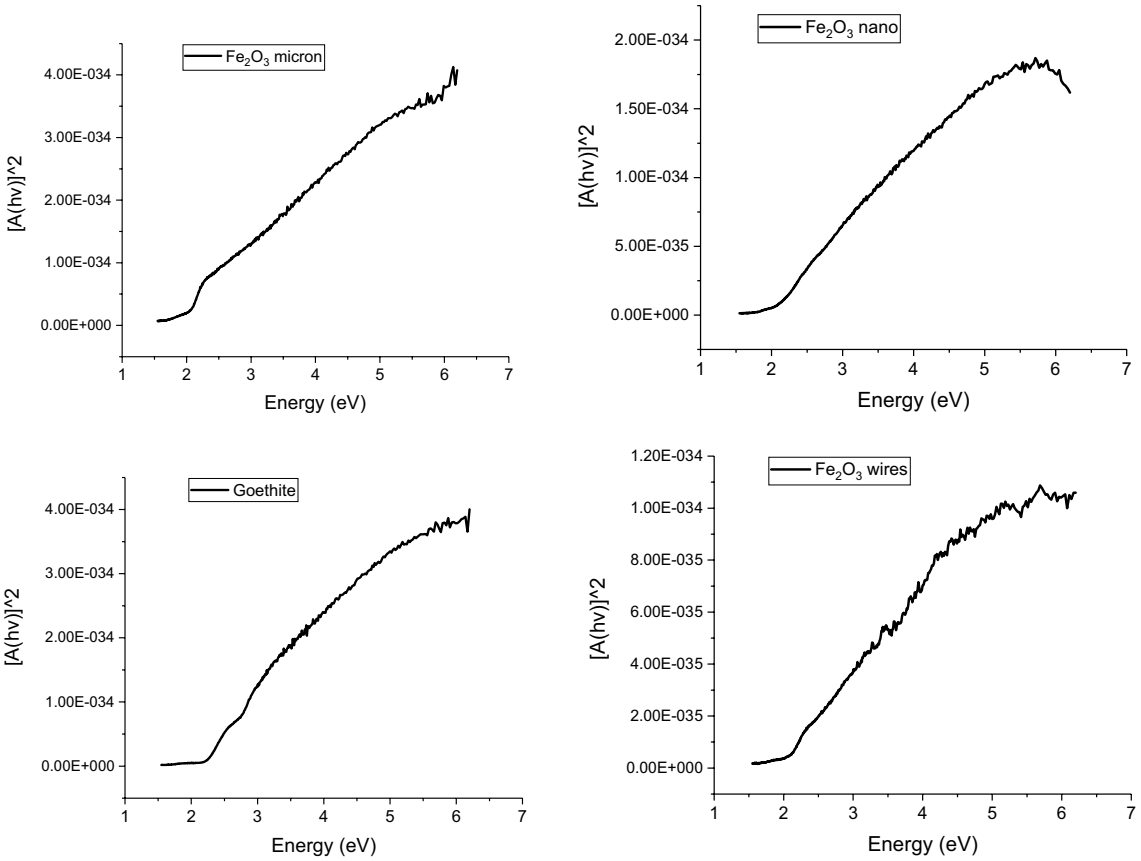

Fig. 4 Kubelka–Munk treated plots of micron- and nano-particulate Fe_2O_3 (top), goethite and Fe_2O_3 wires (bottom)

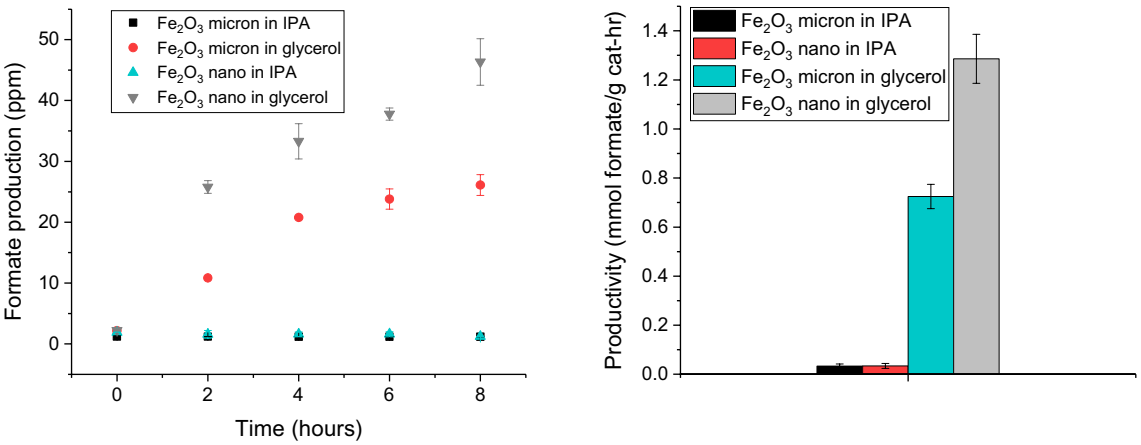

Fig. 5 Formate production in ppm (left) and productivity (right) with micron- and nano-particulate Fe_2O_3 in IPA and glycerol

previous studies, it was found that formate production is pH dependent. At a pH of 8.5, HCO_3^- is the predominant species present, and is therefore expected to be the species undergoing reduction [35]. Figure 5 presents the formate production in ppm and productivity in units of mmol formate/g cat-h for micron- and nano-particulate Fe_2O_3 in two hole scavengers 2-propanol and glycerol. It can be seen that nano-particulate Fe_2O_3 yielded a higher formate production than micron-sized Fe_2O_3, with respective productivities of 0.034 and 0.033 mmol formate/g cat-h in IPA, and 1.29

Table 2 Productivity (mmol formate/g cat-h) of all Fe_2O_3 morphologies in IPA and glycerol

Particle population	Productivity in IPA (mmol formate/g cat-h)	Productivity in glycerol (mmol formate/g cat-h)
Fe_2O_3 micron	0.033 ± 0.001	0.72 ± 0.05
Fe_2O_3 nano	0.034 ± 0.003	1.29 ± 0.11
Goethite	0.042 ± 0.001	0.93 ± 0.02
Fe_2O_3 wires	0.034 ± 0.001	2.79 ± 0.14

All reported values are from triplicate measurements

and 0.72 mmol formate/g cat-h in glycerol (Table 2). Figure 6 presents the production and productivities of goethite, which exhibits similar productivities as micron- and nano-Fe_2O_3 exhibiting slightly higher productivity. Fe_2O_3 wires have the highest productivity of 2.79 mmol formate/g cat-h in glycerol, respectively.

To the best of our knowledge these rates represent the highest production levels reported for bicarbonate conversion to formate using Fe_2O_3 as a photocatalyst. With (Fe_2O_3)* as the photoexcited semiconductor, the proposed redox mechanism of Fe_2O_3 semiconductor photocatalysis is shown in Fig. 7 and Scheme 1. After photoexcitation and the photogeneration of electrons and holes, subsequent reduction of HCO_3^- to HCO_3^{2-} and finally to HCO_2^- takes place. The other half reaction takes place when 2-propanol scavenges photo-generated holes and undergoes oxidation to acetone. With the scavenging of photo-generated holes, this process prolongs charge separation, allowing efficient reduction to take place. To further demonstrate the importance of a hole scavenger, we performed a control experiment without a hole scavenger (Supplementary Information S4). Without the presence of a hole scavenger, formate production does not exceed 2 ppm. This result demonstrates the rapid recombination of charge carriers occurs without a hole scavenger to react with the photo-generated holes. The reduction/oxidation potentials of IPA and glycerol are very similar (IPA 0.80 V and glycerol 0.79 V), so the differences in their efficiencies cannot be explained by their redox potentials alone. Glycerol possesses one secondary and two primary alcohol groups, all of which are potential sites for oxidation. More primary alcohol groups also allow for more efficient C–H hole scavenging. Lastly, glycerol adsorbs better on the surface of Fe_2O_3, which can stabilize the semiconductor in aqueous solution [35]. Based on these reasons, we believe the greater number of alcohol groups in glycerol makes it a superior hole scavenger and therefore results in higher productivities of formate.

Formate production can be quantified in terms of AQE, calculated by Eqs. (1) and (2). As listed in Table 3 the AQEs are extremely low (< 0.1%) when 2-propanol is used as a hole scavenger. In glycerol, micron- and nano-particulate Fe_2O_3 have AQE of 1.45 and 2.57%, respectively. Goethite has a slightly higher AQE of 1.83%, and Fe_2O_3 wires have the highest efficiency of 5.59%. These efficiencies are then compared to commercial TiO_2, which has an AQE of 1.83% (Supplementary Information S5). This finding is an important one because TiO_2 is the benchmark photocatalyst and therefore highlights a low-cost, earth-abundant, and non-toxic alternative that can achieve higher quantum yields. We emphasize the main reason for the Fe_2O_3 nanowires to produce such a high yield of formate is its significantly higher surface area of 90.130 m^2/g. A greater surface area would allow for the better adsorption of bicarbonate

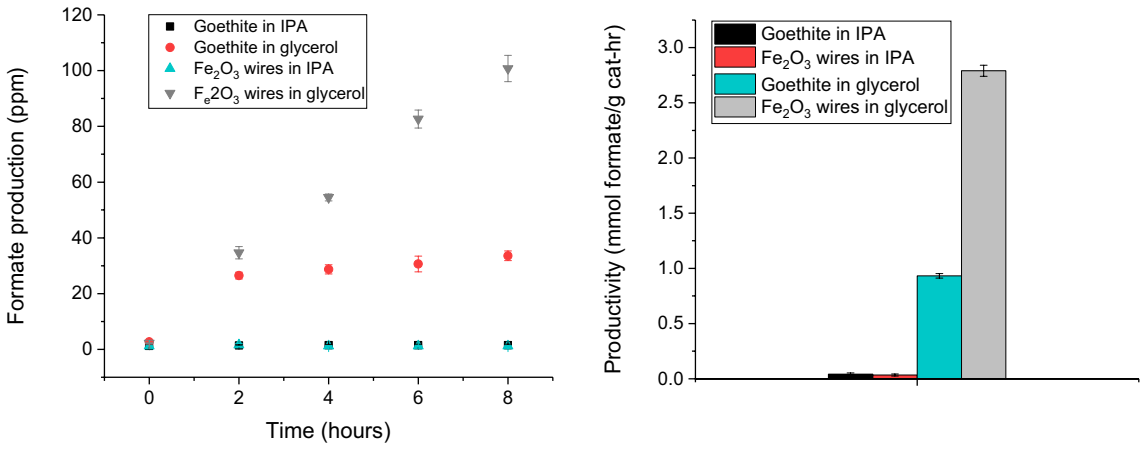

Fig. 6 Formate production in ppm (left) and productivity (right) with goethite and Fe_2O_3 wires in IPA and glycerol

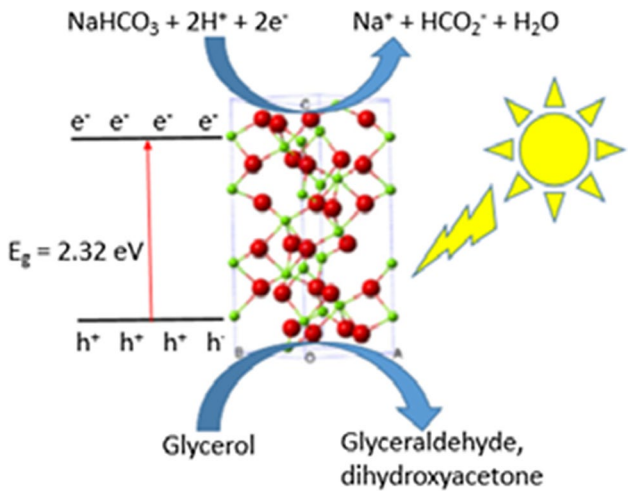

Fig. 7 Proposed mechanism of photocatalytic bicarbonate reduction by Fe_2O_3

Illumination:

$$Fe_2O_3 \xrightarrow{hv} Fe_2O_3{*}(h^+ + e^-)$$

Oxidation:

$$(CH_3)_2CHOH \xrightarrow[(Fe_2O_3)*]{h^+} 2H^+ + (CH_3)_2CO$$

Reduction:

$$HCO_3^- \xrightarrow[(Fe_2O_3)*]{e^-} HCO_3^{2-}$$

$$HCO_3^{2-} \xrightarrow[(Fe_2O_3)*]{2H^+ + e^-} HCO_2^- + H_2O$$

Scheme 1 Proposed mechanism

and glycerol, leading to higher formate productivity. In addition, recombination of photogenerated charge carriers are suppressed due to the intrinsic properties of the nanowires. Fe_2O_3 has short hole diffusion lengths of 2–4 nm, and by constructing one-dimensional Fe_2O_3 wires, recombination can be delayed, resulting in a high yield of formate. Even though the wires exhibited high catalytic efficiency, ~ 95% loss can be attributed to the rapid recombination of photogenerated electron/hole pairs, scattering by the catalyst, hydrogen evolution reaction, and loss of heat.

4 Conclusion

In summary, Fe_2O_3 with different morphologies were synthesized and tested for their catalytic efficiency in the photoreduction of bicarbonate to formate. By exploring the morphology of the semiconductor, we demonstrate that formate production can be greatly increased relative to amorphous systems. One-dimensional Fe_2O_3 wires allow for more efficient photo-generated electron/hole separation, thus resulting in higher photocatalytic activity than the zero-dimensional particles. From the results of this study, Fe_2O_3 bodes well as an earth-abundant, non-toxic, and low-cost semiconductor that possessed higher photocatalytic activity than commercial TiO_2. In addition, we highlight glycerol as a green solvent hole scavenger that boosts photocatalytic efficiency by prolonging charge separation. Future work includes using Fe_2O_3 as a dopant for other semiconductors such as ZnO and TiO_2, and using transient absorption spectroscopy to study charge carrier dynamics. This study portends for fuel production using solar energy and by its regenerative chemical nature should contribute to the increasing important research portfolio necessary towards promoting NETs.

Acknowledgements The authors gratefully acknowledge NSF award # IIA-1301346 for financial support.

Table 3 Summary of semiconductor characterization and apparent quantum efficiency of all Fe_2O_3 morphologies

Particle population	Crystal type	Diameter (μm or nm)	Surface area (m^2/g)	AQE in IPA (%)	AQE in glycerol (%)
Fe_2O_3 micron	Rhombohedral	2 μm	20.384	0.065 ± 0.001	1.45 ± 0.09
Fe_2O_3 nano	Tetragonal	10 nm	37.367	0.069 ± 0.005	2.57 ± 0.2
Goethite	Orthorhombic	2 μm	29.860	0.084 ± 0.02	1.83 ± 0.2
Fe_2O_3 wires	Rhombohedral	5 μm	90.130	0.068 ± 0.002	5.59 ± 0.2

All reported values are from triplicate measurements

Compliance with Ethical Standards

Conflict of interest The authors declare that they have no conflict of interest.

References

1. Fuss S, Reuter WH, Szolgayova J, Obersteiner M (2013) Optimal mitigation strategies with negative emission technologies and carbon sinks under uncertainty. Clim Change 118:73–87
2. Sabine CL, Feely RA, Gruber N, Key RM, Lee K, Bullister JL, Wanninkhof R, Wong CS, Wallace DWR, Tilbrook B, Millero FJ, Peng TH, Kozyr A, Ono T, Rios AF (2004) The oceanic sink for anthropogenic CO_2. Science 305:367–371
3. Lewis N, Nocera D (2006) Powering the planet: chemical challenges in solar energy utilization. Proc Natl Acad Sci USA 103:15729–15735
4. Olah GA, Goeppert A, Surya Prakash GK (2011) Beyond oil and gas: the methanol economy, 2nd edn. Wiley, Somerset
5. Olah GA, Goeppert A, Surya Prakash GK (2009) Chemical recycling of carbon dioxide to methanol and dimethyl ether: from greenhouse gas to renewable, environmentally carbon neutral fuels and synthetic hydrocarbons. J Org Chem 74:487–498
6. Olah GA, Surya Prakash GK, Goeppert A (2011) Anthropogenic chemical carbon cycle for a sustainable future. J Am Chem Soc 133:12881–12898
7. Fujishima A, Honda K (1972) Electrochemical photolysis of water at a semiconductor electrode. Nature 238:37–38
8. Inoue T, Fujishima A, Konishi S, Honda K (1979) Photoelectrocatalytic reduction of carbon dioxide in aqueous suspensions of semiconductor powders. Nature 277:637–638
9. Zhou X, Yang H, Wang C, Mao X, Wang Y, Yang Y, Liu G (2010) Visible light induced photocatalytic degradation of rhodamine B on one-dimensional iron oxide particles. J Phys Chem C 114:17051–17061
10. Mishra M, Chun DM (2015) α-Fe_2O_3 as a photocatalytic material: a review. Appl Catal A 498:126–141
11. Li X, Lin H, Chen X, Niu H, Liu J, Zhang T, Qu F (2016) Dendritic α-Fe_2O_3/TiO_2 nanocomposites with improved visible light photocatalytic activity. Phys Chem Chem Phys 18:9176–9185
12. Cesar I, Kay A, Martinez JAG, Gratzel M (2006) Translucent thin film Fe_2O_3 photoanodes for efficient water splitting by sunlight: nanostructure-directing effect of Si-doping. J Am Chem Soc 128:4582–4583
13. Ohmori T, Takahashi H, Mametsuka H, Suzuki E (2000) Photocatalytic oxygen evolution on α-Fe_2O_3 film using Fe^{3+} as a sacrificial oxidizing agent. Phys Chem Chem Phys 2:3519–3522
14. Gou X, Wang G, Park J, Liu H, Yang J (2008) Monodisperse hematite porous nanospheres: synthesis, characterization, and applications for gas sensors. Nanotechnology 19:125606–125613
15. Zhou H, Wong SS (2008) A facile and mild synthesis of 1-D ZnO, CuO, and alpha-Fe_2O_3 nanostructures and nanostructured arrays. ACS Nano 2:944–958
16. Leland JK, Bard AJ (1987) Photochemistry of colloidal semiconducting iron oxide polymorphs. J Phys Chem 91:5076–5083
17. Dieckmann R (1993) Point defects and transport in haematite (Fe_2O_3). Philos Mag A 68:725–745
18. Jahagirdar AA, Ahmed MNZ, Donappa N, Nagabhushana H, Nagabhushana BM (2014) Photocatalytic degradation of rhodamine B using nanocrystalline α-Fe_2O_3. J Mater Environ Sci 5:1426–1433
19. Wei Q, Zhang Z, Li Z, Zhou Q, Zhu Y (2008) Enhanced photocatalytic activity of porous α-Fe_2O_3 films prepared by rapid thermal oxidation. J Phys D 41:202002–202006
20. Xie J, Zhou Z, Lian Y, Hao Y, Li P, Wei Y (2015) Synthesis of α-Fe_2O_3/ZnO composites for photocatalytic degradation of pentachlorophenol under UV-Vis light irradiation. Ceram Int 41:2622–2625
21. Sun W, Meng Q, Jing L, Liu D, Cao Y (2013) Facile synthesis of surface-modified nanosized α-Fe_2O_3 as efficient visible photocatalysts and mechanism insight. J Phys Chem C 117:1358–1365
22. Kennedy JH, Frese KWJ (1978) Photooxidation of water at α-Fe_2O_3 electrodes. Electrochem Soc 125:709–714
23. Linsebigler AL, Lu G, Yates JT (1995) Photocatalysis on TiO_2 surfaces: principles, mechanisms, and selected results. Chem Rev 95:735–758
24. Huang Y, Ding D, Zhu M, Meng W, Huang Y, Geng F, Li J, Lin J, Tang C, Lei Z, Zhang Z, Zhi C (2015) Facile synthesis of α-Fe_2O_3 nanodisk with superior photocatalytic performance and mechanism insight. Sci Technol Adv Mater 16:1–12
25. Hardee KL, Bard AJ (1976) Semiconductor electrodes V. The application of chemically vapor deposited iron oxide films to photosensitized electrolysis. J Electrochem Soc 123:1024–1026
26. Zhang X, Li H, Wang S, Fan FR, Bard AJ (2014) Improvement of hematite as photocatalyst by doping with tantalum. J Phys Chem C 118:16842–16850
27. Liu H, Wexler D, Wang G (2009) One-pot facile synthesis of iron oxide nanowires as high capacity anode materials for lithium ion batteries. J Alloys Compd 487:L24–L27
28. Maji SK, Mukherjee N, Mondal A, Adhikary B (2012) Synthesis, characterization and photocatalytic activity of α-Fe_2O_3 nanoparticles. Polyhedron 33:145–149
29. Khedr MH, Halim KSA, Soliman NK (2009) Synthesis and photocatalytic activity of nano-sized iron oxides. Mater Lett 63:598–601
30. Lee SC, Lintang HO, Yuliati L (2017) High photocatalytic activity of Fe_2O_3/TiO_2 nanocomposites prepared by photodeposition for degradation of 2,4-dichlorophenoxyacetic acid. J Nanotechnol 8:915–926
31. Bi D, Xu Y (2011) Improved photocatalytic activity of WO_3 through clustered Fe_2O_3 for organic degradation in the presence of H_2O_2. Langmuir 27:9359–9366
32. Hassena H (2016) Photocatalytic degradation of methylene blue by using Al_2O_3/Fe_2O_3 nano composite under visible light. Mod Chem Appl 4:1–5
33. Wang JC, Zhang L, Fang WX, Ren J, Li YY, Yao HC, Wang JS, Li ZJ (2015) Enhanced photoreduction CO_2 activity over direct Z-scheme α-Fe_2O_3/Cu_2O heterostructures under visible light irradiation. ACS Appl Mater Interfaces 7:8631–8639
34. Fang YM, Sun JJ, Wu AH, Su XL, Chen GN (2009) Catalytic electrogenerated chemiluminescence and nitrate reduction at CdS nanotubes modified glassy carbon electrode. Langmuir 25:555–560
35. Leonard DP, Pan H, Heagy MD (2015) Photocatalzyed reduction of bicarbonate to formate: effect of ZnS crystal structure and positive hole scavenger. ACS Appl Mater Interfaces 7:24543–24549
36. Chen S, Wang LW (2012) Thermodynamic oxidation and reduction potentials of photocatalytic semiconductors in aqueous solution. Chem Mater 24:3659–3666
37. Bard AJ, Faulkner LR (2000) Electrochemical methods: fundamentals and applications. Wiley, New York